Quantitative temperature imaging at elevated pressures and in a confined space with CH_4/air laminar flames by filtered Rayleigh scattering*

Bo Yan(闫博)[1,2,3], Li Chen(陈力)[1,2], Meng Li(李猛)[1,2], Shuang Chen(陈爽)[1,2,†], Cheng Gong(龚诚)[2], Fu-Rong Yang(杨富荣)[1,2], Yun-Gang Wu(吴运刚)[1,2], Jiang-Ning Zhou(周江宁)[1,2], and Jin-He Mu(母金河)[1,2]

[1] *Science and Technology on Scramjet Laboratory, Hypervelocity Aerodynamics Institute, China Aerodynamics Research and Development Center, Mianyang* 621000, *China*

[2] *Facility Design and Instrumentation Institute, China Aerodynamics Research and Development Center, Mianyang* 621000, *China*

[3] *College of Aerospace Science and Engineering, National University of Defense Technology, Changsha* 410073, *China*

(Received 28 July 2019; revised manuscript received 22 December 2019; accepted manuscript online 5 January 2020)

Laminar methane/air premixed flames at different pressures in a newly developed high-pressure laminar burner are studied through Cantera simulation and filtered Rayleigh scattering (FRS). Different gas component fractions are obtained through the detailed numerical simulations. And this approach can be used to correct the FRS images of large variations in a Rayleigh cross section in different flame regimes. The temperature distribution above the flat burner is then presented without stray light interference from soot and wall reflection. Results also show that the extent of agreement with the single point measurement by the thermocouple is <6%. Finally, this study concludes that the relative uncertainty of the presented filtered Rayleigh scattering diagnostics is estimated to be below 10% in single-shot imaging.

Keywords: filtered Rayleigh scattering, high-pressure combustion simulator, temperature measurement

PACS: 47.80.Fg, 47.70.Pq, 47.80.Jk, 33.20.Fb **DOI:** 10.1088/1674-1056/ab5f00

1. Introduction

Burner-stabilized flames are still one of the most investigated topics in combustion theory.[1,2] Experiments carried out by a high-pressure laminar combustion burner are widely used to measure flame temperature, speed, structure, and to calibrate optical techniques because of simple geometry and possible access to flame structures.[3] In addition, flames can be efficiently controlled and maintained in different stationary regimes. In this framework, a high-pressure combustion setup comprised of a high-pressure chamber and a McKenna flat burner is installed in our study.[4]

In the course of rapidly evolving engine design and simulation, the demand for obtaining validation temperature data under realistic operating conditions is growing.[5,6] The experimental temperature characterization of aero-thermal flow properties typically relies on probe-based technologies, such as pneumatic multihole devices or thermocouples. Although these conventional probes are readily available and thoroughly tested, most of them are pointwise and contact measurement.

Planar optical measurement techniques, which can cost-effectively provide temperature data, are used to gain insights into complex flow structures spatially and temporally. Planar techniques based on laser-induced fluorescence (LIF)[7,8] and filtered Rayleigh scattering (FRS)[9] techniques are typically used to measure combustion temperature distribution. Generally, LIF technique always uses dual-wavelength to achieve the combustion temperature distribution. However, the realistic combustion situation is usually terrible, such as high pressure, enclosed space and high turbulence and so on. Moreover, a weak LIF signal in a high-pressure environment hinders its development and application in engine combustion diagnosis. As for FRS, the FRS signal can be increased after gas pressure has increased. Moreover, the FRS technique relies on gas molecule scattering only, and no tracing particles are added to the flow. When the laser wavelength is tuned into the filter absorption band, the stray light can be effectively attenuated by a filter cell. Therefore, the FRS technique has been comprehensively explored in the temperature measurement of engine combustion. Doll *et al.* and Schroll *et al.* used this technique to acquire the temperature distribution in a combustion environment simultaneously.[9–12] Successful measurements have also been demonstrated in a high-pressure single-sector combustor and a three-sector combustor. Nevertheless, the FRS technique is susceptible to significant bias errors that result from spatial variation of the mixed gases' Rayleigh cross section.[13]

In this paper, the temperature distribution in a high-pressure laminar burner is achieved by combining the FRS approach and the Cantera simulation. The differences in temperature result and the relative uncertainty between the FRS

*Project supported by the National Natural Science Foundation of China (Grant No. 91641118) and the Fenglei Youth Innovation Fund of China Aerodynamics and Research Development Center, China (Grant Nos. FLYIF20160017 and PJD20180131).

†Corresponding author. E-mail: chenshuang827@gmail.com

technique and the thermocouple are also discussed.

2. Theoretical background

A schematic of the FRS method is shown in Fig. 1. The background scattering light from Mie scattering and the surface reflection light have the same narrow spectral bandwidth, and their frequencies are the same as the frequency of the incident light source.[14,15] However, the Rayleigh scattering intensity profile has a spectral bandwidth of some gigahertz based on a molecule broadening mechanism.[16] An iodine filter that has hyperfine absorption in the vicinity of the incident laser is placed in front of the detector. A strong background scattering light and considerable Rayleigh scattering signals are significantly attenuated by this filter. A sensitive detector is used to collect and accumulate the remaining spectral contributions of Rayleigh signals which pass through the filter, and the important flow information, such as temperature can be deduced from.

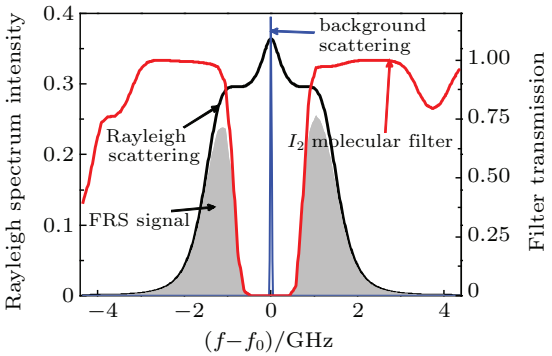

Fig. 1. Plot of Rayleigh spectrum intensity and filter transmission *versus* $f-f_0$.

The intensity collected by the ICCD camera can be described as the convolution of the total spectral intensity and the transmission profile of the iodine filter. The resulting intensity of each ICCD camera pixel element is given by[17,18]

$$S(T,\chi)=CI_0N\sum_k \chi_k\left(\frac{\partial\sigma}{\partial\Omega}\right)_k\int_{\Delta\omega}R_k(w)\tau(\omega,T,M_k)\mathrm{d}\omega, \quad (1)$$

where C denotes the efficiency of the optical setup, and I_0 is the intensity of the illuminating light. The number density of gas molecules is expressed as $N=P/KT$. The total spectral intensity can be described by the sum of the scattering intensities of the k-th gas species. For an assigned gas species, X_k is its mole fraction, M_k is its molecular mass, $\partial\sigma/\partial\Omega$ is the Rayleigh scattering cross section, R_k and τ are the Rayleigh scattering line profile and the transmission profile of the molecular filter, respectively.

A normalized intensity S^* is a function of temperature by normalizing the FRS signal with a measurement taken under normal pressure and temperature condition,[19,20] and expressed as

$$S^*=\frac{S}{S_0}=\frac{T_0}{T}\frac{\sigma_{\mathrm{mix}}(T)}{\sigma_{\mathrm{N_2}}(T_0)}. \quad (2)$$

An FRS cross section for the combustion gas mixture can then be calculated from

$$\sigma_{\mathrm{mix}}(T)=\sum_k X_k\sigma_k(T). \quad (3)$$

In Eq. (3), σ_k is defined as a temperature-dependent FRS cross section for the k^{th} species, and given as

$$\sigma_k(T)=\left(\frac{\partial\sigma}{\partial\Omega}\right)_k\int R_k(\omega,T)\tau(\omega)\mathrm{d}\omega. \quad (4)$$

Finally, the temperature distribution can be determined by identifying the detailed gas components in the combustion area.

3. Experimental facilities

3.1. High-pressure combustion simulator

The experimental study is conducted on a designed high-pressure combustion setup as shown in Fig. 2(a). The setup is cylindrical and composed of stainless steel. The chamber can operate at a maximum pressure of 15 bar (1 bar = 10^5 Pa) and a maximum ambient temperature of 150 °C. The cylindrical chamber has an inner height of 500 mm and an inner diameter of 300 mm. This high-pressure chamber has four view ports positioned at angles of 0°, 90°, 180°, and 270° for a full optical access into the chamber through optical diagnostic techniques. The pressure inside the chamber can be kept constant by electronically regulating the gas flow rate via a back-pressure regulator. The experiments are conducted at steady pressure levels, and the deviation of the pressure from the value set is less than 1%. Monitoring and cooling systems are also equipped in this vessel.

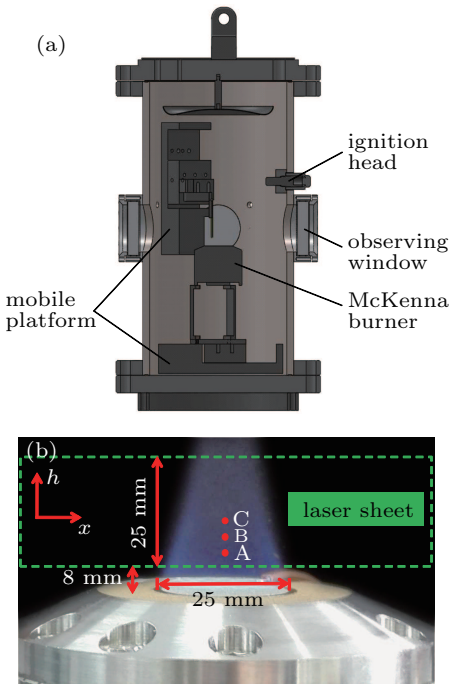

Fig. 2. (a) Schematic diagram of high-pressure burner and (b) size of McKenna burner and experimental layout.

A McKenna flat burner is used to produce the stabilized laminar flames.[21] The gas pipeline diameter of this burner is 25 mm, and the diameter of the whole burner is about 86 mm. Methane (CH_4), nitrogen, and air gas streams are arranged by electronic mass flow controllers. Figure 2(b) shows that CH_4 and air are premixed and then pass through the McKenna flat burner, which creates a highly stable laminar flow. An ignition head above the flat burner is then used to ignite the combustion gas. A thermocouple is also equipped above this burner and can be moved to measure the temperature at different locations above the burner by an electric moving stage. The measuring points in this work are marked as A ($h_A = 13$ mm), B ($h_B = 15$ mm), and C ($h_C = 17$ mm).

3.2. FRS apparatus

A general scheme of the FRS apparatus and the optical arrangement is shown in Fig. 3. The system is comprised of an injection-seeded frequency-doubled Nd:YAG laser, a light sheet system, an iodine cell, an ICCD camera, and a time-controlling device DG535. The output of the laser can be tuned by applying a bias voltage to the heater circuit of the CW seed laser. This tuning capability allows the seeded Nd:YAG to produce the single-frequency green light at 532 nm with a repetition rate of 10 Hz and a narrow spectral linewidth. The laser light is divided into two parts by the beam splitter lens. Then, 1% of laser light is used to detect the laser power and frequency online, and the remaining part is formed into a light sheet to illuminate the region of interest. The width and thickness of this light sheet are 25 mm and 0.5 mm, respectively, as shown in Fig. 2(b). Moreover, the distance between the burner's combustion surface and the light sheet bottom is $h_0 = 8$ mm. Rayleigh scattering from the combustion is then imaged through an iodine filter cell (I_2 gas temperature is 52.3 °C, and the I_2 cell transmission curve is shown in Fig. A1 in Appendix A), and a narrow linewidth filter onto a intensified CCD camera.

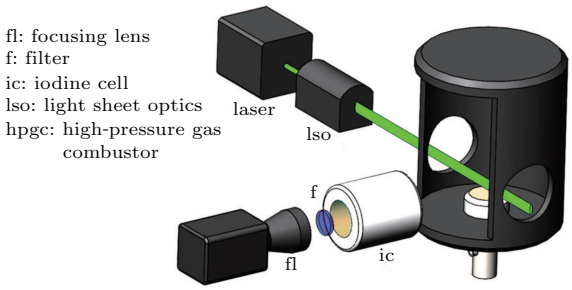

Fig. 3. Principal setup and optical arrangement of FRS system.

4. Results and discussion

4.1. One-dimensional simulation

Three cases with different operating pressures are considered in the present study. The flow rates, the equivalence ratio Φ, and the premixed gas velocity premixed for the different conditions are shown in Table 1.

Table 1. Parameters of McKenna flat flames: chamber pressure p, flow rates of air through burner Q_{Air}, CH_4 fuel Q_{CH_4}, equivalence ratio Φ, premixed gas velocity $v_{premixed}$, and component fraction of N_2: $X(N_2)$, O_2: $X(O_2)$, CO_2: $X(CO_2)$, H_2O: $X(H_2O)$. Flow rate in standard liters per minute (slm) refers to the flow rate under 1.013 bar and 273 K.

	p/MPa	Q_{CH_4}/SLM	Q_{Air}/SLM	Φ	$v_{premixed}$/(cm/s)	$X(N_2)$	$X(O_2)$	$X(CO_2)$	$X(H_2O)$
Case 1	0.14	0.7	7	0.95	18.68	71.81%	0.92%	9.07%	18.11%
Case 2	0.4	0.8	8	0.95	7.48	71.79%	0.94%	9.03%	18.11%
Case 3	0.88	1.1	11	0.95	4.67	71.73%	1.00%	8.91%	18.00%

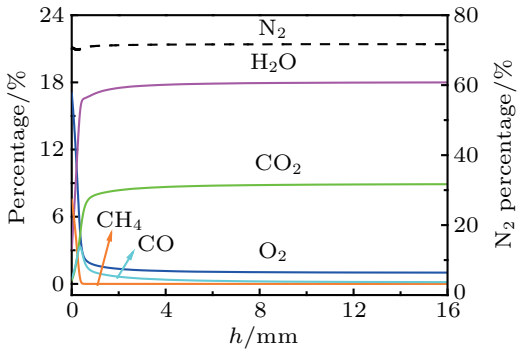

Fig. 4. Different component fractions for case 2 (Table 1) simulated by Cantera.

The laminar flame structures under the experimental conditions are first investigated by using one-dimensional simulation. The simulations are carried out by using Cantera, which is an open-source suite of tools for problems involving chemical kinetics, thermodynamics and transport processes. A mechanism with 53 species and 325 reactions (GRI-3.0) is adopted for the chemical kinetics. In the one-dimensional simulations, the inlet was set to be at a fixed temperature and gas compositions; the pressure in the domain is set to be constant following the experimental conditions.

The major composition mole fractions along the axis from the simulations are plotted in Fig. 4. It is shown that changes of the major compositions are limited in a short region near the inlet ($h \approx 0.5$ mm), which corresponds to the reaction zone in the flame. In the chemical reaction region ($h < 0.5$ mm), the mole fractions of the production compositions (H_2O and CO_2) increase as the height h improves; while the mole fractions of the reactants (CH_4, O_2) decrease. The intermediate composition (CO) increases from the inlet and reaches a maximum value at the reaction zone. On the downstream side of the reaction zone ($h > 0.5$ mm), the mole fractions of the composi-

tions remain nearly stable,which corresponds to the so-called post flame region of the flame. According to this analysis, we can conclude that the measuring region (h = 8 mm–33 mm) in the present experiments is in the post flame zone, in which the composition changes due to the fact that the reactions can be neglected. Therefore, the mole fractions of the major compositions in the post flame zone can be considered as those detailed in Table 1, and those out of the flame is covered by N_2.

4.2. FRS calibration analysis

The ability to remove the stray light interference from soot and wall reflection is analyzed as shown in Figs. 5 and 6. The air Rayleigh scattering image with and without the filter cell are obtained (see Fig. 5). The strong primary reflection of the light sheet reflecting from the probe and from the wall are both clearly visible. However, when the frequency of the laser is tuned to the minimal transmission through the molecular filter, the strong elastic stray light of the primary reflex is absorbed by the molecular filter. Rayleigh scattering, which is due to being illuminated by the laser light sheet, becomes visible.

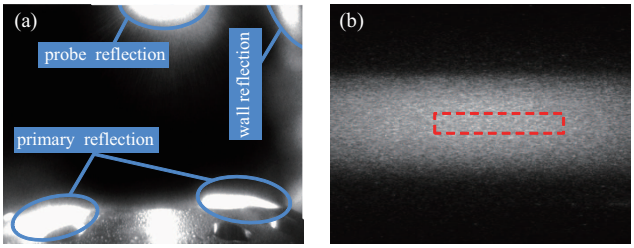

Fig. 5. Scattering image (a) without and (b) with iodine filtering cell.

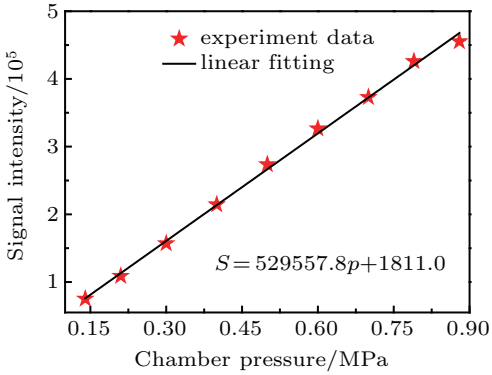

Fig. 6. Relation between Rayleigh scattering signal intensity S and chamber pressure p.

A total of 50 laser shots are typically captured at different pressures, and the average values calculated in the red dashed line area (Fig. 5(b)) are shown in Fig. 6. A linear formula is used to fit the Rayleigh scattering signals at different pressures to obtain the stray light interference. Moreover, the Rayleigh scattering intensity is $S \propto p$, because $S \propto N$ and $N = pV/RT$, where N is the gas density, p is the chamber pressure, and T is the gas temperature. The fitting process results in 1811 for the intercept value introduced by the stray light. Therefore, the interference from the stray light can decrease to 3% by adding the iodine filter.

The intensity of the FRS signal is dependent on scattering cross section and Rayleigh profile of the scattering molecules as shown in Section 2. Typical cross sections are shown in Table B2 in Appendix B. In addition, the intensity and spectral profile of the scattering are needed to deduce the temperature, and several Rayleigh–Brillouin scattering profiles are calculated by S7 model (Tenti),[22,23] and the results are shown in Fig. B1 in Appendix B.

Then, the transmission of the iodine filter (see Fig. A1 in Appendix A) multiplied with the Rayleigh–Brillouin scattering profiles results in a specific intensity for all gas species as shown in Fig. B1 in Appendix B. From Figs. 4 and B2, we can see that N_2 is the predominant component in the gas because of its high concentration in air; however, CO_2 also affects the FRS signal due to its high Rayleigh cross section compared with the H_2O molecule. Finally, the normalized intensity ratio ($S(T)/S_0$) is calculated with considering the effective Rayleigh cross section of N_2 and CO_2 as shown in Fig. 7. Thus, if the ratio is known the temperature can be determined.

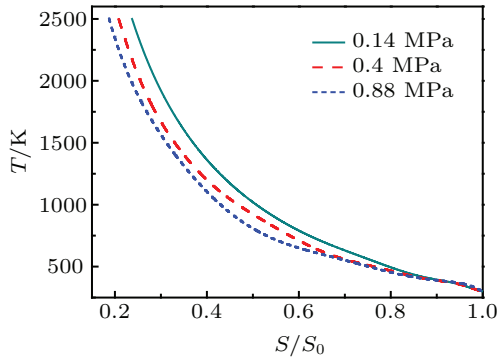

Fig. 7. Intensity ratio-dependent temperatures measured by using FRS at different pressures.

4.3. Flame shape and temperature measurements

The flat laminar flame temperature distribution above the McKenna flat burner is then measured by the FRS apparatus, and the results are shown in Fig. 8. The parameters of burner measurement are detailed in Subsection 4.1. The larger the value of p is, the sharper the flame shape is and the narrower the flame section is. This trend is due to the decrease in the premixed gas volume per unit time with the value of p increasing. Figure 9 also shows the temperature distribution at h = 15 mm above the burner. The temperature profiles of the three cases are similar in shape on the whole. Temperature steeply rises, then becomes constant, and finally symmetrically decreases. The maximum temperature in the flat roof increases with the pressure rising. The relative uncertainty at different pressures and mean temperatures are also calculated. The relative uncertainty at 0.14 MPa and 1500 K is approximately 11% and decreases as the mean temperature

decreases and the pressure improves, because of the increase of the Rayleigh scattering signal.

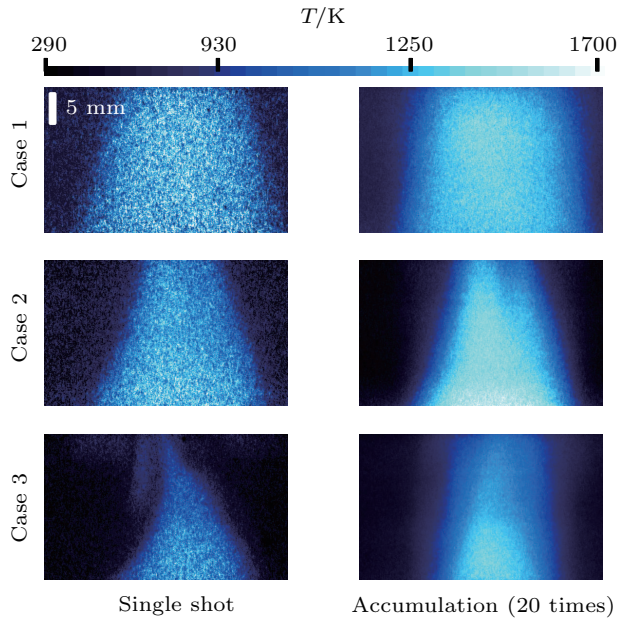

Fig. 8. Single-shot and multiple-shot images of combustion temperature distribution at different pressures, measured by FRS technique.

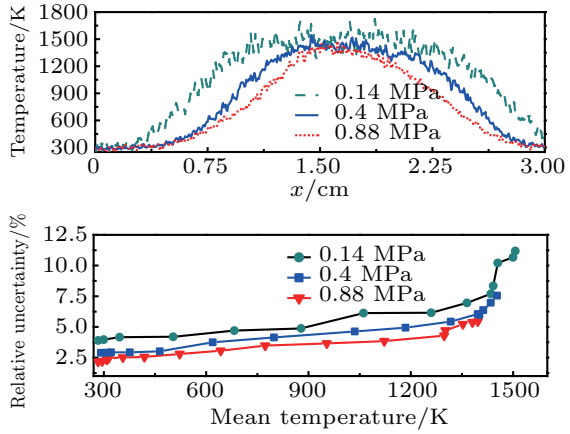

Fig. 9. (a) Distributions of combustion temperature (single shot) at 1.5 cm above the burner; (b) variations of relative uncertainty with mean temperature based on Fig. 9.

The temperatures above the burner, measure by the FRS technique and by the thermocouple are compared with each other as shown in Fig. 10, and the measuring points are marked in Fig. 2(b). Three prominent features are observed in Fig. 10. First, the temperatures from the two techniques clearly decrease as h increases mainly because heat is lost due to the inflating N_2 gas around the flame. Second, the two techniques present a declining temperature trend as p increases because the premixed gas velocity decreases (Table 1). Third, at point A, the discrepancy between FRS and the thermocouple can be directly reduced by increasing the value of p. Specifically, the discrepancy becomes 5.3%, 3.7%, and 2.8% when p is 0.14 MPa, 0.4 MPa, and 0.88 MPa, respectively. By contrast, a small discrepancy can be obtained at low height and low temperature. The Rayleigh scattering intensity is strengthened by enhancing p and h. Consequently, the strengthened intensity increases the accuracy of the FRS technique.

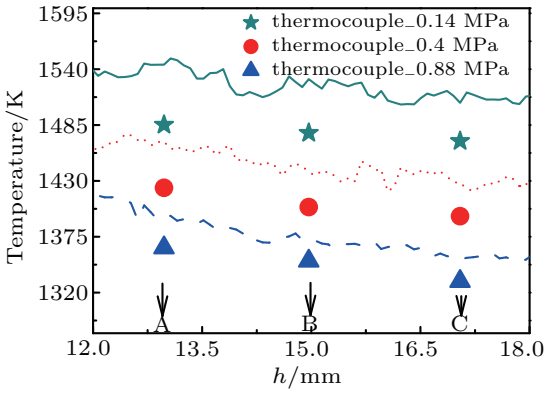

Fig. 10. Comparison between temperature results obtained from FRS technique (averaging 50 times) and thermocouple.

5. Conclusions and perspectives

In this study, the thermocouple and the FRS technique are used to obtain the temperature distribution in a high-pressure gas combustor with CH_4/air flames. Three operating conditions, namely, p of 0.14 MPa, 0.4 MPa, and 0.88 MPa, are investigated. The axial composition distributions corresponding to the different conditions are modeled by Cantera simulations. Further FRS experiments show the temperature distribution above the McKenna burner. The relative uncertainty and discrepancy between the results obtained from the thermocouple and the FRS technique decrease as the chamber pressure increases. The FRS technique can be used to measure turbulent flame in some complicated engines, such as internal combustion and scramjet engines, by further improving the systematic sampling rate based on a laser and a CCD camera.

Appendix A: I_2 transmission profiles

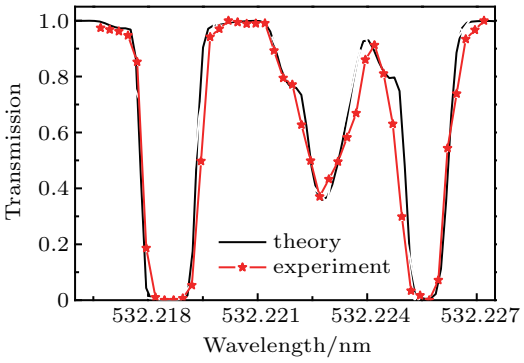

Fig. A1. Theoretical and experimental transmission curve of I_2 cell at around 532.2185 nm.

Appendix B: Rayleigh scattering cross sections and profiles

Table B1 shows the Rayleigh scattering cross sections of different gas species at 532 nm. The Rayleigh cross section of CO_2 is the biggest, and that of N_2 is the second biggest.

The Rayleigh cross section of H_2O is less than those of the other species, such as Air and O_2. Therefore, for the other reaction products such as CO_2 and H_2O, we can attribute the influence of FRS signal to the Rayleigh scattering of CO_2 due to its higher Rayleigh cross section than that of H_2O.

Table B1. Differential Rayleigh scattering cross sections of combustion-related species at 532 nm.

Species	Air	N_2	O_2	CO_2	H_2O (vapor)
Rayleigh cross section $(\partial/\partial\Omega) \times 10^{-28}$ cm^2	5.87	6.11	5.04	13.9	4.36

The N_2 and CO_2 Rayleigh scattering profiles simulated by S7 model[22,23] are graphically shown in Fig. B1. At the atmospheric pressure, N_2 Rayleigh spectrum can be considered as the Gauss profile. The higher the temperature, the wider the Rayleigh spectrum broadening is, due to the aggravation of the intermolecular collision. Furthermore, as the pressure increases, the interaction between the incident laser and the acoustic wave strengthens, resulting in the symmetrical Brillouin peaks appearing on both sides of the Rayleigh peak. Meanwhile, the intensity of Brillouin peak overtakes that of Rayleigh peak as the pressure further increases.

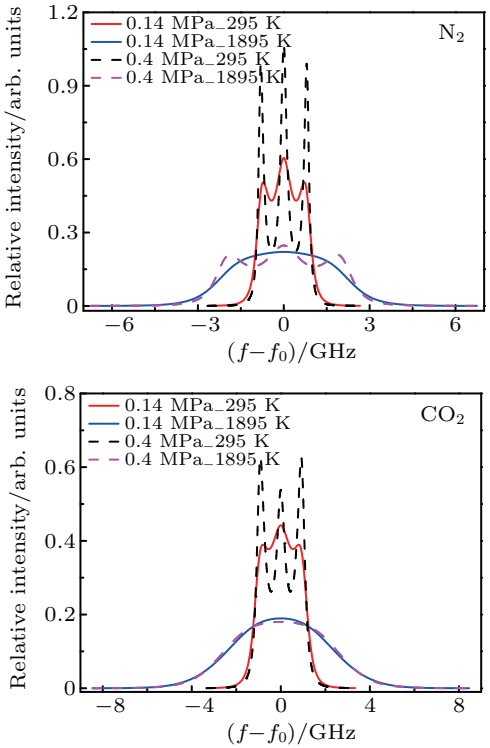

Fig. B1. Rayleigh–Brillouin scattering profiles of N_2 and CO_2 at different temperatures and pressures.

Finally, the transmission of the iodine filter (see Fig. A1) multiplied with the Rayleigh–Brillouin scattering profile (see Fig. B1) results in a specific intensity for all gas species as shown in Fig. B2. The relative intensity of CO_2 is also bigger than those of the other gas species (N_2, H_2O, and O_2).

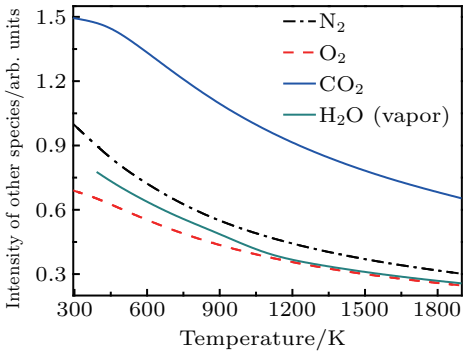

Fig. B2. Variations of relative intensity with temperature for several species, considering relevant Rayleigh scattering cross sections for N_2 at 1.4 atm and 295 K. The unit 1 atm = 1.01325×10^5 Pa.

References

[1] Most D and Leipertz A 2001 *Appl. Opt.* **40** 5379
[2] Zetterberg J, Li Z, Afzelius M and Aldén M 2008 *Appl. Spectrosc.* **62** 778
[3] Liu J R, Hu Z Y and Zhang Z R 2011 *Opt. Percision Eng.* **19** 284
[4] Hu S, Gao J, Gong C, Zhou Y, Bai X S, Li Z S and Alden M 2018 *Appl. Energy* **227** 149
[5] Fourguette D C, Zurni R M and Long M B 1986 *Combust. Sci. Technol.* **44** 307
[6] Peterson B, Baum E, Böhm B, Sick V and Dreizler A 2013 *Proceedings of the Combustion Institute* **34** 3653
[7] Mcmillin B K, Palmer J L, Seitzman J M and Hanson R 1993 31*th Aiaa Aerospace Sciences Meeting and Exhibit,* January 11–14, Reno, Nv, USA, p. 0044
[8] Seitzman J M, Palmer J L and Antonio A L 1993 31*th Aiaa Aerospace Sciences Meeting and Exhibi,* January 11–14, Reno, Nv, USA, p. 0802
[9] Elliot G S and Glumac N 1999 37*th Aiaa Aerospace Sciences Meeting and Exhibit*, January 11–14, Reno, Nv, USA, p. 0643
[10] Doll U, Fischer M, Stockhausen G and Willett C 2012 16*th Int. Symp. on Applications of Laser Techniques to Fluid Mechanics,* July 9–12, Lisbon, Portugal
[11] Doll U, Stockhausen G and Willert C 2017 *Opt. Lett.* **42** 3773
[12] Schroll M, Doll U, Stockhausen G, Meier U, Willert C, Chris H, Christoph B and Bagchi I 2017 *J. Eng. Gas. Turb. Power* **139** 011503
[13] Sean P K, Robert W S, Steven J B and Thomas 2005 *Appl. Opt.* **44** 1548
[14] Elliott G S, Glumac N, Carter C D and Nejad A S 1997 *Combust. Sci. Technol.* **125** 351
[15] Vieitez M O, van Duijn E J, Ubachs W, Witschas B, Meijer A, de Wijn A S, Dam N J and Water W 2010 *Phys. Rev. A* **82** 043836
[16] Miles R B, Lempert W R and Forkey J N 2001 *Meas. Sci. Thchnol.* **12** 33
[17] Forkey J 1996 "Development and Demonstration of Filtered Rayleigh Scattering: a Laser Based Flow Diagnostic for Planar Measurement of Velocity, Temperature and Pressure", Ph. D. Dissertation (New Jersey: Princeton University)
[18] Pitz R, Cattolica R, Robben F and Talbot L 1976 *Combust. Flame* **27** 313
[19] Elliott G S, Glumac N and Carter C D 2001 *Meas. Sci. Thcnnol.* **12** 452
[20] Kearney S P, Schefer R W, Beresh S J and Grasser T W 2005 *Appl. Opt.* **44** 1548
[21] Sutton G, Levick A, Edwards G and Greenhalgh D 2006 *Combust. Flame* **147** 39
[22] Tenti G, Boley C D and Desai R C 1974 *Can. J. Phys.* **52** 285
[23] Pan X, Shneider M N and Miles R B 2004 *Phys. Rev. A* **69** 33814